Simpson Fiona (Orcid ID: 0000-0001-7589-115X)

# Nowcasting and validating Earth's electric-field response to extreme space-weather events using magnetotelluric data: application to the September 2017 geomagnetic storm and comparison to observed and modelled fields in Scotland

Fiona Simpson[1,*] and Karsten Bahr[2]

[1,*]*School of Ocean and Earth Science, University of Southampton, UK*

[2]*Institut für Geophysik, Georg-August Universität, Göttingen, Germany.*

Corresponding author: Fiona Simpson (f.simpson@soton.ac.uk)

**Key Points:**

- Comparison of techniques for nowcasting electric fields during magnetic storms.
- Validation against electromagnetic data recorded in Scotland during the September 2017 magnetic storm.
- Presentation of method for correcting impedance tensors for horizontal magnetic field gradients to improve electric-field nowcasting.

This article has been accepted for publication and undergone full peer review but has not been through the copyediting, typesetting, pagination and proofreading process which may lead to differences between this version and the Version of Record. Please cite this article as doi: 10.1029/2019SW002432

## Abstract

In the UK, geomagnetically induced currents (GICs) are calculated from thin-sheet electrical conductivity models. In the absence of conductivity models, time derivatives of magnetic fields are sometimes used as proxies for GIC-related electric fields. An alternative approach, favored in the US, is to calculate storm-time electric fields from time-independent impedance tensors computed from an array of magnetotelluric (MT) sites and storm-time magnetic fields recorded at geomagnetic observatories or assumed from line-current models. A paucity of direct measurements of storm-time electric fields has restricted validation of these different techniques for nowcasting electric fields and GICs. Here, we present unique storm-time electric-field data from 7 MT sites in Scotland that recorded before, during and after the September 2017 magnetic storm. By Fourier transforming electric-field spectra computed using different techniques back to the time domain, we are able to make direct comparisons with these measured storm-time electric-field time series. This enables us to test the validity of different approaches to nowcasting electric fields. Our preferred technique involves frequency-domain multiplication of magnetic-field spectra from a regional site with a local impedance tensor that has been corrected for horizontal magnetic-field gradients present between the local site and the regional site using perturbation tensors derived from geomagnetic depth sounding (GDS). Scatter plots of scaling factors between measured and nowcasted electric fields demonstrate the importance of coupling between the polarization of the storm-time magnetic source field and Earth’s direction-dependent deep electrical conductivity structure.

## Plain Language Summary

The Sun emits a constant stream of charged particles that interact with the Earth’s magnetic field in complex ways. Sometimes, heightened solar activity in the form of coronal mass ejections results in extreme fluctuations of Earth’s magnetic fields called magnetic storms. Time-varying magnetic fields associated with magnetic storms induce electric fields within the Earth, the magnitudes of which depend on Earth’s electrical conductivity structure. These electric fields are potentially hazardous to our power distribution and communication networks, because they drive quasi-dc currents along their electrically-conductive transmission lines. Therefore, several governments around the world are prioritizing research into nowcasting and forecasting the ground-based impacts of magnetic storms. However, at present, there is little storm-time electric-field data available against which to compare the electric fields that we nowcast from our models. Here, we use simultaneous recordings of the electric and magnetic fields during the 8th September 2017 magnetic storm to investigate how closely electric fields nowcasted using different techniques match those observed. We use this comparative study to assess the most advantageous approach to nowcasting and forecasting electric fields.

## 1 Introduction

The magnetotelluric (MT) sounding technique (Tikhonov, 1950, reprinted 1986; Cagniard, 1953) involves measuring and cross-correlating natural fluctuations in the electric and magnetic fields that are induced in the Earth due to solar-magnetosphere-ionosphere interactions. As a geophysical technique, MT is primarily used to constrain the conductivity structure of the Earth's crust and upper mantle following computation of period-dependent impedance tensors from cross-correlated horizontal components of the induced electromagnetic fields (e.g., Simpson and Bahr, 2005):

$$\begin{pmatrix} E_\mathrm{x} \\ E_\mathrm{y} \end{pmatrix} = \begin{pmatrix} Z_\mathrm{xx} & Z_\mathrm{xy} \\ Z_\mathrm{yx} & Z_\mathrm{yy} \end{pmatrix} \begin{pmatrix} B_\mathrm{x}/\mu_0 \\ B_\mathrm{y}/\mu_0 \end{pmatrix} \tag{1}$$

Where $\boldsymbol{E}$ denotes electric field, $\boldsymbol{B}$ denotes magnetic field, $\boldsymbol{Z}_\mathrm{ij}$ denotes impedance and x and y are orthogonal directions in the horizontal plane at the Earth's surface.

However, the nature of the passive MT source field means that MT also lends itself to the study of space weather by providing information about the electric fields that drive geomagnetically induced currents (GICs) that are potentially hazardous (e.g., Boteler, 2003; Cannon et al., 2013) to power grids (e.g., Bolduc, 2002; Radasky, 2011; Pulkinnen et al., 2017), gas pipelines (Gummow et al., 2002; Viljanen et al., 2006) and railway networks (Krausmann et al., 2015). From equation (1), we see that if we already know the MT impedance tensor at a range of periods from previous measurements and have magnetic-field data during a magnetic storm from a geomagnetic observatory, we can calculate the electric fields that would be induced by the magnetic storm – i.e., we can negate the need for continuous, long-term, electric-field measurements once we have determined the impedance tensor at a range of periods. This range of periods is approximately 1 s - $10^5$ s (e.g., Simpson and Bahr, 2005). At periods shorter than 1 s, the electromagnetic source field is dominated by ionospheric activity such as lightning rather than solar-magnetosphere-ionosphere interactions; at periods longer than $10^5$ s, the source field becomes non-uniform and time-dependent even during solar-quiet times (e.g., Simpson, 2002), violating the plane-wave assumption of the MT method. The plane-wave assumption is also more likely to be violated during magnetic storms, when the source field becomes more complex. However, at mid-latitudes, the storm-time source field is dominated by the ring current, the wavelength associated with the spatial heterogeneity of magnetic storms is an order of magnitude longer than the penetration depth at the longest period and source-field heterogeneities are expected to be of second-order importance compared to variations in the Earth's 3D electrical conductivity structure, which encompass several orders of magnitude (e.g., Simpson et al., 1997; Simpson, 2000; Simpson and Bahr, 2005).

The magnetic-field fluctuations show less spatial variation than the induced electric fields. Therefore, time-dependent magnetic-field variations from a geomagnetic observatory can often be used as a proxy for magnetic-field variations at neighboring sites. However, in the presence of geomagnetic anomalies, the magnetic field will also be modified. In this case, the induced electric fields across a region will not be correctly estimated using the impedance tensor and geomagnetic observatory data only, because it is necessary to correct for horizontal magnetic-field gradients between the geomagnetic observatory and neighboring sites where the impedance tensor is known. This correction can be incorporated using transfer functions obtained from geomagnetic depth sounding (GDS). GDS is a technique that is complementary to MT for investigating the electrical conductivity structure of the Earth

(Simpson and Bahr, 2005). GDS utilizes the horizontal and vertical components of the fluctuating magnetic field, to obtain a perturbation tensor, $\boldsymbol{W}$ (Schmucker, 1970) that relates the magnetic-field components at a local measurement site (subscript L) to those at a simultaneously-recording reference or observatory site (subscript O):

$$\begin{pmatrix} B_{\mathrm{Lx}} \\ B_{\mathrm{Ly}} \\ B_{\mathrm{Lz}} \end{pmatrix} - \begin{pmatrix} B_{0\mathrm{x}} \\ B_{0\mathrm{y}} \\ B_{Oz} \end{pmatrix} = \begin{pmatrix} w_{\mathrm{xx}} & w_{\mathrm{xy}} \\ w_{\mathrm{yx}} & w_{\mathrm{yy}} \\ w_{z\mathrm{x}} & w_{zy} \end{pmatrix} \begin{pmatrix} B_{0\mathrm{x}} \\ B_{0\mathrm{y}} \\ B_{Oz} \end{pmatrix} \tag{2}$$

GDS transfer functions can be computed at no extra cost from MT time series. The impedance tensor correction for the anomalous magnetic field between a geomagnetic observatory and an MT measuring site is derived in the next section (Methods). We note similarities in our approach to Schultz and Bonner (2017). However, our MT array data (Simpson and Bahr, 2020) from the 8th September 2017 magnetic storm provides a unique opportunity to validate the correction procedure.

According to Faraday's Law, a time-varying magnetic field induces closed loops of electric fields around an axis oriented parallel to the inducing field:

$$\nabla \times \boldsymbol{E} = -\frac{\partial \boldsymbol{B}}{\partial t} \tag{3}$$

Hence, it has been suggested (e.g., Viljanen et al., 2001; Pulkkinen et al., 2006; Watermann and Gleisner, 2009) that time derivatives of storm-time magnetic fields might have a role to play in forecasting GIC-related electric fields. For example, in the idealized scenario of a 1-D Earth, equation (3) reduces to:

$$\frac{\partial B_{\mathrm{x}}}{\partial t} = \frac{\partial E_{\mathrm{y}}}{\partial z} \tag{4a}$$

$$-\frac{\partial B_{\mathrm{y}}}{\partial t} = \frac{\partial E_{\mathrm{x}}}{\partial z} \tag{4b}$$

Therefore, for a 1D approximation, time derivatives of the horizontally-polarized magnetic fields are equal to the vertical gradients of the perpendicularly-polarized electric fields. However, the greater regional uniformity of magnetic fields compared to electric fields raises doubts about the efficacy of $\partial \boldsymbol{B}/\partial t$ for forecasting GICs.

Increasing awareness of the potential socio-economic effects (e.g., OECD, 2018; Eastwood et al., 2018) of magnetic-storm-related damage to ground-based infrastructure has spawned a plethora of scientific papers concerned with modelling GICs in different geographic regions (e.g., Viljanen et al., 2012; Bedrosian and Love, 2015; Lucas et al., 2018; Bonner and Schultz 2017; Espinosa et al., 2019; Love et al., 2019; Marshall et al., 2019; Rosenquist and Hall, 2019). However, because large magnetic storms occur infrequently and site occupation times for most MT surveys targeting crustal structure typically range from 1-2 days to 2-3 weeks, the statistical chances of recording a severe geomagnetic storm during a typical MT survey are low. Therefore, it has not been possible to compare and validate different approaches to generating hazard maps (e.g., Love et al., 2016) and models (e.g., Viljanen et al., 2012; Lucas et al., 2018) of space-weather impacts on ground-based infrastructure against empirical measurements of storm-time electromagnetic fields. Here, we present an analysis of a unique electromagnetic dataset (Simpson and Bahr, 2020) recorded during the 8th September 2017 magnetic storm at 7 MT sites in the Scottish Highlands (Figure 1) and explore how well we can reproduce the electric fields measured during the storm using different techniques.

## 2 Methods

### 2.1 Data acquisition

We recorded 5-component ($H_x$, $H_y$, $H_z$, $E_x$ and $E_y$) continuous, electromagnetic time series at 7 sites (Figure 1) in northern Scotland during the 8th September 2017 geomagnetic storm (Simpson and Bahr, 2020). We employed low-noise, Magson magnetometers and non-polarizable silver-silver-chloride electrodes (Filloux, 1987) that were buried to a depth of 0.5 m to mitigate against temperature-related fluctuations and drift. Impedance tensors and perturbation tensors were computed (e.g., Egbert and Booker, 1986; Simpson and Bahr, 2005) from MT data collected intermittently over a duration exceeding 3 months at sites chosen for their remoteness from population centers and are, therefore, well-constrained to periods up to 30 000 s. The need for such long periods has been discussed by Bonner and Schultz (2017). Although electric and magnetic fields fluctuate with time, for stable tectonic environments, the bivariate impedances calculated from them can be considered stationary (e.g., Hanekop and Simpson, 2006). Therefore, it is not critical which time windows are used to calculate the MT impedances, with the caveat that storm times should be avoided because of an increased likelihood that the plane-wave assumption of the MT method (e.g., Simpson and Bahr, 2005) is violated at such times.

### 2.2 Objectives and data analysis

Our objectives in this paper are to compare the measured electric-field responses (Simpson and Bahr, 2020) at any particular site during the September 2017 storm with:

a) The electric field determined from the local MT impedance tensor (Equation 1) at that site multiplied in the frequency domain with (i) the magnetic-field spectra recorded during the storm at the same observation site; (ii) the magnetic-field spectra at site RAN; (iii) the magnetic-field spectra at RAN with a correction to the impedance tensor that takes into account anomalous geomagnetic fields between RAN and the observation site, as described by the perturbation tensor (Equation 2). We will refer to this approach as "electric fields determined from local impedance tensors".

b) The electric field determined from frequency-domain multiplication of the magnetic-field spectra recorded during the storm (Simpson and Bahr, 2020) at the MT site of interest with an MT impedance modelled (Siripunvaraporn et al., 2002; Siripunvaraporn et al., 2005) assuming (i) a 100-Ωm half-space; (ii) a 100-Ωm half-space plus 3D near-surface conductance of the ocean surrounding the UK; (iii) a 900-Ωm half-space; (iv) a 900-Ωm half-space plus 3D near-surface conductance of the ocean surrounding the UK. We will refer to this approach as "electric fields determined from modelled impedance tensors". The resistivity of seawater is assumed to be 0.25 Ωm and the maximum depth of the modelled ocean is 4 km.

c) Time derivatives of the horizontal magnetic fields measured simultaneously at the same sites (Simpson and Bahr, 2020) during the storm.

Time-series analyses were performed by (i) Fourier transformation of the requisite magnetic field into the frequency domain; (ii) convolution with the appropriate impedance tensor to calculate electric-field spectra; (iii) Fourier transformation of the spectra back to the time domain for plotting as time series that could be compared with the measured time series. We decimated the electromagnetic time series to a cadence of 32 s and used window-lengths of 1024 data points for our Fourier evaluation. We also present frequency-domain scatter plots of univariate and bivariate scaling factors between measured and nowcasted electric fields from objectives a) and b). Others (e.g., Love et al., 2016; Kelbert et al., 2017) have previously convolved measured impedance tensors with magnetic-field spectra to investigate electric-field spectra at particular frequencies during magnetic storms, but validation has only previously been undertaken using 3 long-duration electric-field measurements from Japan (Kelbert et al., 2017).

### 2.3 Correction for horizontal magnetic-field gradients

To derive the correction required by the substitution of the measured magnetic field at a site with the magnetic field from a neighboring site (in our case RAN), we consider two sites O and L, where O is a geomagnetic observatory site and L is a local site where the MT impedance is available. In MT, the orthogonal components of the horizontal electric and magnetic fields measured at the two sites, O and L are related via complex impedance tensors, $\mathbf{Z}_{\mathrm{O}}$ and $\mathbf{Z}_{\mathrm{L}}$:

$$\boldsymbol{E}_{\mathrm{L}} = \boldsymbol{Z}_{\mathrm{L}}\boldsymbol{B}_{\mathrm{L}}/\mu_0 \tag{5a}$$

$$\boldsymbol{E}_{\mathrm{O}} = \boldsymbol{Z}_{\mathrm{O}}\boldsymbol{B}_{\mathrm{O}}/\mu_0 \tag{5b}$$

The GDS transfer function between O and L is given by the relation:

$$\boldsymbol{B}_{\mathrm{L}} - \boldsymbol{B}_{\mathrm{O}} = \boldsymbol{W}\boldsymbol{B}_{\mathrm{O}} \tag{6}$$

Where, for the purposes of our study, we are only interested in the horizontal magnetic fields – i.e., vertical magnetic fields can be neglected.

From equation 6, the magnetic field at the observation site L is obtained to be:

$$\boldsymbol{B}_{\mathrm{L}} = \boldsymbol{W}\boldsymbol{B}_{\mathrm{O}} + \boldsymbol{B}_{\mathrm{O}} = (\boldsymbol{W} + \mathbf{1})\boldsymbol{B}_{\mathrm{O}} \tag{7}$$

The magnetic field at site L can then be substituted into equation 5 to obtain:

$$\boldsymbol{E}_{L} = \boldsymbol{Z}_{L}(\boldsymbol{W} + \mathbf{1})\,\boldsymbol{B}_{\mathrm{O}}/\mu_0 \tag{8}$$

Where $\boldsymbol{W}$ is the perturbation tensor from equation 2, without the vertical elements $w_{zx}$ and $w_{zy}$. Therefore, when substituting magnetic fields from a regional site, O (such as a geomagnetic observatory) at a local site, L, where an impedance tensor, $Z_L$, is known, a correction factor of $(\mathbf{W}+\mathbf{1})$ is required to be applied to $Z_L$ in order to account for horizontal magnetic fields between O and L before estimating electric fields. For a larger dataset, covering a larger region, a multi-station approach (Zhang and Schultz, 1990; Bonner and Schultz, 2017) might be preferable. Unfortunately, there are gaps in the geomagnetic time series from the nearest geomagnetic observatory at Eskdalemuir (ESK: 55.32°, -3.2°) from 1st September - 9th September 2017. So, our localized, temporary, MT array (Simpson and Bahr, 2020) provides the only measured geomagnetic data available for the 8th September 2017 storm in Scotland.

## 3 Results

### 3.1 Measured electromagnetic fields

Horizontal magnetic and electric fields recorded (Simpson and Bahr, 2020) during the 8th September 2017 storm are shown in Figures 2 and 3. Comparison of these fields confirms that the magnetic fields show significantly less spatial (i.e., site-to-site) variability than the electric fields. In particular, the north-south ($E_x$) component of the electric fields at site LEA is significantly smaller than the electric fields at other sites, whilst the east-west ($E_y$) component is larger than at all other sites with the exception of ACH. This diminution of the $E_x$ electric fields at LEA is attributable to strong polarization of the electric fields in one direction due to current channeling (Bahr, 1991). The difference in spatial variability between the magnetic fields and induced electric fields demonstrates the significant effect of the Earth's 3D electrical conductivity structure on the form of the storm-time electric fields. However, some differences in magnetic-field magnitude are evident in Figure 2. For example, magnetic fields at ACH are larger than at RAN.

Impedance tensors and their confidence intervals for 4 sites (TAN, MAR, LEA, RAN; Figure 1) calculated from MT data collected before and after the 8th September 2017 storm are shown in Figure 4. These serve to show the data quality and the frequency bandwidth available for nowcasting electric fields. Horizontal magnetic-field gradients are quantified in the perturbation tensor, $\boldsymbol{W}$ (Figure 5). Site RAN was chosen as the reference magnetic-field ($\boldsymbol{B}_O$, Equation 2) site, because the MT impedances indicate that the electrical conductivity structure is less complex with regard to current channeling and dimensionality in the vicinity of RAN than at other sites.

Measured storm-time electric fields (Simpson and Bahr, 2020) are significantly larger at ACH than at other sites (Figure 3; Table 1). There is no obvious explanation for this, but we speculate that it could be due to current channeling along a nearby railway line. We also observe that the electric fields at site LEA are strongly polarized (Bahr, 1991), with weak $E_x$ fields and large $E_y$ fields (Figure 3; Table 1). We attribute this strong polarization to the proximity of site LEA to the Great Glen Fault (Kennedy, 1946) that can be seen as a green valley cutting diagonally across the Highlands on Figure 1.

### 3.2 Time-domain analyses

#### 3.2.1 Electric fields nowcasted from local impedance tensors

Figure 6 compares the electric fields obtained from method a) (see Section 2.2 of Methods). At MAR, there is a qualitatively good agreement between the measured fields and those computed using the local impedance tensor and either local magnetic fields or those from RAN (Figure 6a). However, from Table 1, we see that the nowcasted electric fields are mostly smaller than the measured ones. This diminution in maximum peak-to-peak magnitude of the electric field is most pronounced in $E_x$ when magnetic fields from RAN are substituted for those at MAR without making a correction for anomalous magnetic fields. Application of the perturbation-tensor correction in this case results in a significant improvement in the agreement between the maximum peak-to-peak electric-field magnitudes determined from the magnetic fields at RAN and MAR. However, the nowcasted fields for both $E_x$ and $E_y$ polarizations are only about 75% of the measured ones. At TAN, nowcasted $E_x$ fields are consistently smaller than the measured ones, whereas nowcasted $E_y$ fields are consistently larger than the measured ones (Table 1). However, the time series exhibit similar forms (Figure 6b). The discrepancy between measured and nowcasted electric fields at TAN is most pronounced when magnetic fields from RAN are substituted for the local magnetic fields at TAN with no perturbation-tensor correction. In this case, application of the perturbation-tensor correction improves the agreement between the maximum peak-to-peak electric-field magnitudes nowcasted from the local magnetic fields at TAN and substituted fields from site RAN. At site LEA, nowcasted $E_x$ fields are significantly larger than the measured ones, whereas $E_y$ fields nowcasted from the local magnetic field at LEA are 85% of the measured ones (Table 1). We attribute this to strong polarization of telluric currents at this site as discussed in Section 3.1. The characteristic peak oscillation between 01:00 and 02:00 hours (just under half way through the recording window shown) seen in all other time series traces (Figure 5) is not pronounced in the $E_x$ fields measured at LEA. Again, application of the perturbation-tensor correction improves the agreement between the maximum peak-to-peak $E_y$ electric-field magnitudes nowcasted from the local magnetic fields at LEA and substituted fields from site RAN. However, there is a poor agreement between nowcasted and measured $E_x$ fields at this site.

The measured electric (Figure 3) and magnetic (Figure 2) fields at ACH are larger than at any other site. $E_x$ fields nowcasted at ACH are significantly smaller than the measured ones (Table 1). Substitution of the magnetic field from RAN for the local magnetic field from ACH produces maximum peak-to-peak $E_y$ magnitudes that are in excellent agreement with the measured ones, whereas maximum peak-to-peak $E_y$ magnitudes nowcasted from the local magnetic-field spectra at ACH are significantly overestimated compared to the measured ones (Table 1). Application of the perturbation-tensor correction at ACH has a less significant effect than at other sites (Table 1), suggesting that these observations are not due to anomalous regional magnetic-field gradients present in the perturbation tensor.

In Section 3.3.1, we will perform univariate and bivariate analyses in the frequency domain to further investigate the discrepancies between measured and nowcasted electric fields evident in Table 1. This will allow us to decompose the time-series data into its constituent frequencies and compute average scaling factors between measured and nowcasted electric fields from the resulting scatter plots. This will provide insight into the processes involved.

### 3.2.2 Electric fields nowcasted from modelled impedance tensors

We investigated the effect of ocean bathymetry on the MT impedances using the 3D forward modelling code of Siripunvaraporn et al. (2005). Synthetic impedances for individual site locations in models consisting of either i) a 100-Ωm half-space; ii) a 900-Ωm half-space; (iii) 3D ocean bathymetry underlain by a 100-Ωm half-space; iv) 3D ocean bathymetry underlain by a 900-Ωm half-space were multiplied with measured magnetic-field spectra from the relevant site in the frequency domain to obtain electric-field spectra. The resistivity of seawater was assumed to be 0.25 Ωm and the maximum depth of the modelled ocean was 4 km. The electric-field spectra were Fourier transformed into the time domain to allow for comparison with measured electric-field time series.

Comparing measured electric fields at MAR and ACH (Simpson and Bahr, 2020) with those nowcasted from modelled impedances, we find a generally poor agreement between measured and nowcasted maximum peak-to-peak electric-field magnitudes (Table 2) and the forms of the time-series traces (e.g., Figure 7). This is in agreement with a synthetic modelling study performed by Bedrosian and Love (2015). Maximum peak-to-peak electric-field magnitudes are approximately 3 times greater for the case of a 900-Ωm half-space than a 100-Ωm half-space. This is to be expected since apparent resistivity $\rho_a$ is dependent on $\left|Z_{ij}\right|^2$ according to (e.g., Simpson and Bahr, 2005):

$$\rho_{\mathrm{a,ij}}(\omega) = \left|Z_{ij}(\omega)\right|^2 / \omega\mu_0 \tag{9}$$

Where $\omega$ is angular frequency.

Comparing results in Table 2, we find that the effect of ocean bathymetry is greater for the model containing a 900-Ωm half-space compared to the model containing a 100-Ωm half-space. This is to be expected since a subsurface of higher resistivity provides less shielding from lateral conductivity anomalies, resulting in a larger horizontal adjustment length (Ranganayaki and Madden, 1980) for electromagnetic fields of a given wavelength.

In a previous study aimed at modelling GICs in the UK power network, Beggan et al. (2013) used a 900-Ωm half-space to represent the conductivity of the upper crust, lower crust and mantle below a thin sheet representing the conductance of an ocean up to 4-km deep surrounding the UK. However, below the upper crust, electrical resistivity is generally significantly less than 900-Ωm (e.g., Simpson and Warner, 1998; Simpson, 1999; Simpson, 2002) and our results (Figure 7; Table 2) show that the magnitudes and orientations of electric fields and therefore GIC magnitudes are likely to be misrepresented by Beggan et al.'s model. Inclusion of near-surface conductance due to ocean bathymetry does not improve the agreement between the measured and nowcasted electric-field responses at our sites. For the model containing a 100-Ωm half-space, inclusion of 3D ocean bathymetry has no significant effect on the nowcasting of $E_x$ at MAR, TAN and RAN or $E_y$ at any of the 5 sites. We therefore consider the effect of ocean bathymetry to be insignificant compared to the Earth's deep conductivity structure embodied in the MT impedance tensor for the sites studied. As shown by other MT studies (e.g., Simpson, 2000; Sakkas et al., 2002; Simpson, 2002; Kelbert et al., 2012), the electrical conductivity of the Earth can vary by several orders of magnitude, not just at the interfaces between continents and oceans, but also across tectonic boundaries and mantle discontinuities. These electrical conductivity variations have been shown to be of first-order importance in space-weather studies conducted in the US (e.g., Meqbel et al., 2014). As the ocean surrounding the UK is shallow compared to the thickness of the crust and mantle, variations in the conductivity of the Earth's crust and mantle, rather than the conductance of the ocean will dominate the long-period MT response.

Comparison of the model results in Table 2 also demonstrates sensitivity to the magnetic-field spectra chosen for frequency-domain multiplication with impedance, since for our half-space model, the impedance used for the calculation is the same at each site. For example, nowcasted peak-to-peak electric-field magnitudes for $E_y$ are approximately twice as big at ACH compared to TAN, which is consistent with the larger $B_x$ fields measured at ACH compared to TAN (Figure 2). These examples show the necessity of ensuring that assumptions related to spatial variations in magnetic source fields are valid before a regional magnetic field is used for nowcasting electric fields at any given location. We will further investigate the scaling factors between measured and modelled electric fields using univariate and bivariate frequency-domain analyses in Section 3.3.2.

### 3.2.3 Are time derivatives of magnetic fields effective proxies for electric fields?

We calculated the time derivatives of the horizontally-polarized magnetic fields (Figure 8). Comparing the times series in Figure 8 with the electric fields for the same storm-time window shown in Figure 3 demonstrates that peak-to-peak electric-field magnitudes are substantially more spatially variable than would be inferred from the time derivatives of the magnetic fields.

We, further, find that substantially different scaling factors are evident between the peak values of the horizontal time derivatives of the magnetic fields and the corresponding measured peak-to-peak electric-field magnitudes (Table 1) for the north-south and east-west polarizations at individual sites and that scaling factors for neighboring sites, particularly for the north-south polarization are significantly different (Table 3). We attribute these different scaling factors to multi-dimensionality of the subsurface electrical conductivity structure in Scotland leading to spatial gradients and direction-dependence of the induced electric fields that can only be adequately investigated if MT impedances are available. As the field costs of an MT survey are similar to the costs of magnetovariational surveys, we suggest that the $\partial \boldsymbol{B}/dt$ technique (and other techniques relying purely on magnetic variations) should be considered obsolete for space-weather forecasting in favor of the direct, simultaneous measurements of electric and magnetic fields provided by the MT technique. Similar ambiguity is present when using horizontal magnetic gradients, which provide relative but not absolute information about electric-field scaling factors and conductivity variations – i.e., magnetovariational techniques cannot substitute the need for electric-field measurements.

## 3.3. Univariate and bivariate analyses in the frequency domain

### 3.3.1 Comparison of measured and nowcasted electric-field spectra

The nowcasted peak-to-peak electric fields in Table 1 are mostly underestimates of the measured values. Therefore, we investigate the ratio of nowcasted to measured electric fields in the frequency domain at frequencies between 0.015 Hz and 0.000124 Hz (64 s to 8200 s). We use MT processing techniques that average neighboured raw spectra (Simpson and Bahr, 2005) to estimate the transfer functions *a* and *b* between the nowcasted electric fields (subscript "(now)") and the measured electric fields (subscript "(meas)"):

$$E_{\mathrm{x\,(now)}} = aE_{\mathrm{x\,(meas)}} \tag{10a}$$

$$E_{\mathrm{y\,(now)}} = bE_{\mathrm{y\,(meas)}} \tag{10b}$$

Whereas, for the estimation of impedance tensors, spectra from multiple time windows are stacked, the 8th September 2017 storm covers only one time window (Figures 2 and 3). Therefore, the numbers of degrees of freedom (numbers of independent information) for each evaluation frequency is smaller for *a* than for $\boldsymbol{Z}$. However, the average scaling factors obtained using univariate analysis (Figure 9; Table 4) are similar to the underestimated scaling factors that we obtained in the time domain (Table 1). We, therefore, also calculated scaling factors for a bivariate analysis:

$$E_{\mathrm{x\,(now)}} = a_2 E_{\mathrm{x\,(meas)}} + b_2 E_{\mathrm{y\,(meas)}} \tag{11a}$$

$$E_{\mathrm{y\,(now)}} = c_2 E_{\mathrm{x\,(meas)}} + d_2 E_{\mathrm{y\,(meas)}} \tag{11b}$$

$$e = (a_2 + b_2)^{1/2} \tag{12a}$$

$$f = (c_2 + d_2)^{1/2} \tag{12b}$$

The bivariate scaling factors, *e* and *f*, tend to be slightly larger than unity and therefore yield nowcasted electric fields that are overestimates of the measured ones. The averages of the scaling factors $a$ and $e$ or $b$ and $f$ obtained from the univariate and bivariate analysis is close to unity, with the remaining discrepancies – i.e., departures from a scaling factor of 1 – attributable to the limited numbers of degrees of freedom.

A possible source of the existence of a correlation between orthogonal, nowcasted and measured, electric-field components lies in differences between the polarizations of the magnetic fields used in the analysis: whereas the impedance tensors are estimated from the Fourier coefficients obtained from several time windows with arbitrary polarizations of the magnetic field, the storm-time magnetic field is strongly polarized. For example, the magnetic field of the classic ring current model has only a $B_x$ (and $B_z$) component but no $B_y$ component. This is not the case for the 8th September 2017 storm in Scotland, for which the magnetic fields (Figure 2) are NNW-SSE polarized. When this polarization interacts with the direction-dependent conductivity of the mantle, non-vanishing transfer functions ($b_2$ and $d_2$) between orthogonal components of the nowcasted and measured electric fields are created in addition to the dominant transfer functions ($a_2$ and $c_2$) describing the scaling factors between the parallel components of the nowcasted and measured electric fields.

From the summary of the frequency-domain estimation of the scaling factors between nowcasted and measured electric fields in Table 4 we see that the scaling factors are closest to unity when the local magnetic fields measured at the MT sites are used. For the case that the magnetic field of site RAN is substituted for the local magnetic field at any particular site, the perturbation-tensor correction mostly produces scaling factors closer to the ones using local magnetic fields than those derived from uncorrected impedance tensors.

### 3.3.2 Comparison of measured and modelled electric-field spectra

We conducted similar univariate and bivariate analyses to those described in Section 3.3.1 on electric fields nowcasted using impedances synthesised using the models incorporating the 3D conductance of the ocean described in Section 3.2.2. For models containing a 100-Ωm half-space, the $E_x$-polarized electric fields are significantly too small (Figure 10b). For models containing a 900-Ωm half-space, the $E_y$-polarized electric fields are significantly too large (Figure 10c) and the scatter of the data points is significantly greater than observed in the measured data (Figure 10a).

## 4 Discussion and Conclusion

Severe magnetic storms are infrequent and short-lived events. The magnetic fields associated with them can be analyzed quantitatively using data from a global network of geomagnetic observatories, but long-term, continuous measurements of induced electric fields are less readily available. This means that models and techniques used to infer the magnitudes of induced electric fields and GICs associated with magnetic storms have not been extensively validated against measured electric-field data from the region to which they are applied.

Without adequate validation (see also Kelbert et al., 2017), we cannot be sure that hazard maps (e.g., Love et al., 2016) showing the risk that GICs present to technological infrastructure are correct. MT data recorded in Scotland before, during and after the September 2017 magnetic storm (Simpson and Bahr, 2020) have provided a unique opportunity to compare measured storm-time electromagnetic time series with electric-field time series synthesized using different techniques. We have compared electric fields measured during the 8th September 2017 storm with those determined by multiplying electromagnetic transfer functions and magnetic-field spectra, considering both impedance tensors and perturbation tensors derived from MT data and synthetic impedance tensors derived using 1D and 3D modelling.

Although horizontal magnetic-field gradients in Scotland are low (e.g., Figure 5), we find that application of a perturbation-tensor correction to the measured impedance tensor to account for horizontal magnetic-field gradients when using magnetic-field spectra from a site other than the local site where the impedance tensor has been measured improves the agreement between the measured and the nowcasted electric fields. We, therefore, suggest that perturbation tensors should be calculated routinely alongside impedance tensors for the purpose of investigating space-weather impacts. This is particularly desirable for regions (unlike Scotland) with strong horizontal magnetic gradients.

Comparing measured and nowcasted, peak-to-peak, electric-field values from local impedance tensors in Table 1, we find that some nowcasted values are over-estimates, whereas others are under-estimates of the measured values. Scatter plots of scaling factors between measured and nowcasted electric fields from univariate and bivariate analyses in the frequency domain (Figure 9) have enabled us to attribute some of the discrepancies observed to coupling between the polarization of the storm-time magnetic source field and the direction-dependence of Earth's deep electrical-conductivity structure. Other possible causes of misfit between measured and nowcasted electric fields have been discussed by Kelbert et al. (2017). These include cultural noise, filtering effects, storm-time departures from the plane-wave assumption of the MT method, induction in the oceans (particularly tidal harmonics), current channeling, multi-dimensionality of Earth's subsurface, conductivity structure and static shift (e.g., Simpson and Bahr, 2005). However, the average nowcasted peak-to-peak magnitude is close to the average measured value. Therefore, it is desirable to calculate geomagnetic induced currents (GICs) from electric fields averaged over a regional array of MT sites to mitigate statistical biases due to local effects that commonly distort electric fields. As determination of voltages from which GICs are calculated involves integrating electric fields over transmission-line lengths, interpolation across an array of sites is anyway desirable.

We find that 1D and 3D modelling techniques based on assumed models (e.g., Kappenman, 2004; Boteler and Pirjola, 2017) that ignore the Earth's deep electrical conductivity structure (e.g., Simpson and Warner, 1998; Simpson, 2002) do not provide an acceptable degree of agreement between nowcasted and measured electric fields. We conclude that techniques of this kind are significantly inferior to techniques that rely on measured impedance tensors that contain all information about Earth's 3D conductivity structure. For our particular sites located inland from shallow seas, coast effects are found to be less significant than Earth's deep conductivity structure.

We have also demonstrated that time derivatives of magnetic fields are of limited value compared to direct measurements of electric fields. As has also been discussed by Bonner and Schultz (2017), only MT impedances, uncorrected for static distortion effects (e.g., Simpson and Bahr, 2005) can provide information about absolute scaling factors for local electric fields.

Long-duration electromagnetic time series and long-period MT impedances are necessary pre-requisites for any approach to nowcasting and validating models of extreme space-weather effects on ground-based technological infrastructure. If the ultimate aim is to forecast these effects, then the models on which forecasts are based must first be validated. However, the database of storm-time electric-field measurements is limited. Based on the results of our validation study using electric and magnetic fields measured during the September 2017 magnetic storm (Simpson and Bahr, 2020), we recommend basing risk assessments for vulnerability to extreme space-weather events on measured impedance tensors, perturbation tensors and magnetic-field spectra. We suggest that this approach is likely to be more robust than techniques relying on indirect inferences about storm-time electric fields from overly simplistic electrical conductivity models or time derivatives of magnetic fields.

Our bivariate, frequency-domain analyses have also highlighted the importance of the polarization of the storm-time electric field. This demonstrates that for the purpose of forecasting the effects of extreme space-weather events, it is not sufficient to forecast magnetic-field magnitudes – two storms with similar magnitudes, but different polarizations could pose very different hazards to ground-based infrastructure in a given region. The analyses that we have presented are only possible because of the availability of electromagnetic data recorded during a magnetic storm (Simpson and Bahr, 2020). Therefore, longer-term, continuous electromagnetic recordings are recommended in order to enhance the likelihood of capturing further spatially and temporally coincident electric- and magnetic-field data during future magnetic storms.

## Acknowledgments and Data

This work was supported by the Natural Environment Research Council (NERC Grant NE/P016782/1). We thank Forestry Commission Scotland, National Trust for Scotland and Glen Tanar Estate for allowing us to install MT instrumentation on their land. We also thank Adam Schultz and an anonymous reviewer for thoughtful reviews that helped us to improve an earlier version of our manuscript. Electromagnetic data recorded by the authors before, during and after the September 2017 storm are available in Simpson and Bahr (2020).

## References

Bahr, K. (1991). Geological noise in magnetotelluric data: a classification of distortion types. *Phys. Earth Planet. Inter.*, *66*, 24-38. https://doi.org/10.1016/0031-9201(91)90101-M

Bedrosian, P. A. and Love, J. J. (2015). Mapping geoelectric fields during magnetic storms: synthetic analysis of empirical United States impedances, *Geophys. Res. Lett.*, *42*, 10160-10170. https://doi.org/10.1002/2015GL066636

Beggan, C., Beamish, D., Richards, A., Kelly, G. and Thomson, A. W. P. (2013). Prediction of extreme geomagnetically induced currents in the UK high-voltage network, *Space Weather*, *11*, 407-419. https://doi.org/10.1002/swe20065

Bolduc, L. (2002). GIC observations and studies in the Hydro- Québec power system. *J. Atmos. Solar-Terr. Phys.*, *64*, 1793-1802. https://doi.org/10.1016/51364-6826(02)00128-1

Bonner, L. R and Schultz, A. (2017). Rapid prediction of electric fields associated with geomagnetically induced currents in the presence of 3D ground structure. Projection of remote magnetic observatory data through MT impedance tensors. *Space Weather*, *15*, 204-227. https://doi.org/10.1002/2016SW001535

Boteler, D. H. (2003). Geomagnetic hazards to conducting networks. *Natural Hazards*, *28*, 537-561. https://doi.org/10.1023/A:1022902713136

Boteler, D. H. and Pirjola, R. J. (2017). Modelling geomagnetically induced currents. *Space Weather*, *15*, 258-276. https://doi.org/10.1002/2016SW001499

Cagniard, L. (1953). Basic theory of the magnetotelluric method of geophysical prospecting. *Geophysics*, *15*, 123-157.

Cannon, P., Angling, M., Barclay, L., Curry, C., Dyer, C., Edwards, R., Green, G., Hapgood, M., Horne, R. B., Jackson, D., Mitchell, C. N., Owen, J., Richards, A., Rogers, C., Ryden, K., Saunders, S., Sweeting, M., Tanner, R., Thomson, A. and Underwood, C. (2013). *Extreme space weather impacts on engineered systems and infrastructure*. UK Royal Academy of Engineering, pp. 69. ISBN: 1-903496-95-0

Eastwood, J. P., Hapgood, M. A., Biffis, E., Benedetti, D., Bisi, M. M., Green. L., Bentley, R. D. and Burnett, C. (2018). Quantifying the economic value of space weather forecasting for power grids: an exploratory study. *Space Weather*, *16*, 2052-2067. https://doi.org/10.1029/2018SW002003

Egbert, G. D. and Booker, J. R. (1986). Robust estimation of geomagnetic transfer functions. *Geophys. J. R. Astr. Soc.*, *87*, 173-194. https://doi.org/10.1111/j.1365-246X.1986.tb04552.x

Espinosa, K. V., Padhila, A. L. and Alves, L. R. (2019). Effects of ionospheric conductivity and ground conductance on geomagnetically induced currents during geomagnetic storms: case studies at low-latitude and equatorial regions. *Space Weather*, *17*, 252-268. https://doi.org/10.1029/2018SW002094

Filloux, J. H. Instrumentation and experimental methods for oceanic studies. In *Geomagnetism, Volume 1*, ed. J. A. Jacobs. London: Academic Press, pp. 143-248, 1987, ISBN: 9780123786715.

Gummow, R. A. (2002). GIC effects on pipeline corrosion and corrosion control systems. *Journal of Atmospheric and Solar-Terrestrial Physics*, *64*, 1755-1764. https://doi.org/10.1016/51364-6826(02).00125-6

Hanekop, O. and Simpson, F. (2006). Error propagation in electromagnetic transfer functions: what role for the magnetotelluric method in detecting earthquake precursors? *Geophys. J. Int.*, 165, 763-774. https://doi.org/10.1111/j.1365-246X.2006.02948.x.

Kappenman, J. G. (2004). Space weather and the vulnerability of electric power grids. In *Effects of Space Weather on Technology Infrastructure*, ed. Daglis, I. A., Kluwer Academic Publishers, Netherlands, pp. 257-286. https://doi.org/10.1007/1-4020-2754-0_14

Kelbert, A., G. D. Egbert, and C. deGroot-Hedlin (2012). Crust and upper mantle electrical conductivity beneath the Yellowstone Hotspot Track, *Geology*, 40(5), 447–450. https://doi.org/10.1130/G32655.1

Kelbert, A., Balch, C. C., Pulkkinen, A., Egbert, G. D., Love, J. J., Rigler, E. J., & Fujii, I. (2017). Methodology for time-domain estimation of storm time geoelectric fields using the 3-D magnetotelluric response tensors. *Space Weather*, *15*(7), 874-894. https://doi.org/10.1002/2017SW001594

Kennedy, W. Q., 1946. The Great Glen Fault. *Quarterly Journal of the Geological Society*, London, *102*, pp. 41-76. https://doi.org/10.1144/GSL.JGS.1946.102.01-04.04

Krausmann, E., Andersson, E., Russel, T. and Murtagh, W. (2015). Space weather and rail: findings and outlook. *EU Joint Research Centre report*, Publications Office of the EU, Luxembourg, pp. 29. https://doi.org/10.2788/211456

Love, J. J., Lucas, G. M., Bedrosian, P. A. and Kelbert, A. (2019). Extreme-value geoelectric amplitude and polarization across the Northeast United States. *Space Weather*, *17*, 379-395. https://doi.org/10.1029/2018SW002068

Love, J., Pulkinnen, A., Bedrosian, P., Jonas, S., Kelbert, A., Rigler, E. J., Finn, C., Balch, C. C., Rutledge, R., Waggel, R. M., Sabata, A. T., Kozyra, J. U., Black, C. E. (2016). Geoelectric hazard maps for the continental United States. *Geophys. Res. Lett.*, *43*, 9415-9424. https://doi.org/10.1002/2016GL070469

Lucas, G. M., Love, J. J. and Kelbert, A. (2018). Calculation of voltages in electric power transmission lines during historic geomagnetic storms: An investigation using realistic earth impedances. *Space Weather*, *16*, 185-195. https://doi.org/10.1002/2017SW001779

Marshall, R. A., Wang, L., Paskos, G. A., Olivares-Pulido, G., Van der Walt, T., Ong, C., Mikkelsen, D., Hesse, G., McMahon, B., Van Wyk, E., Ivanovich, G., Spoor, D., Taylor, C. and Yoshikawa, A. (2019). Modeling geomagnetically induced currents in Australian power networks using different conductivity models, *Space Weather*, *17*, 727-756. https://doi.org/10.1029/2018SW002047

Meqbel, N., Egbert, G., Wannamaker, P., Kelbert, A. and Schultz, A. (2014). Deep electrical resistivity structure of the Pacific NW derived from 3-D inversion of Earthscope US Array magnetotelluric data. *Earth Plan. Sci. Lett*., **402**, https://doi.org/10.1016/j.epsl.2013.12.026

OECD (2018). National risk assessments: a cross country perspective. *OECD Publishing*, Paris https://doi.org/10.1787/9789264287532-en

Pulkkinen, A., Viljanen, A. and Pirjola, R. (2006). Estimation of geomagnetically induced current levels from different input data. *Space Weather*, *4*, https://doi.org/10.1029/2006SW000229

Pulkkinen, A., Bernabeu, E., Thomson, A., Viljanen, A., Pirjola, R., Boteler, D., Eichner, J., Cilliers, P. J., Welling, D., Savani, N. P., Weigel, R. S., Love, J. J., Balch, C., Ngwira, C. M., Crowley, G., Schultz, A., Kataoka, R., Anderson, B., Fugate, D., Simpson, J. J. and

MacAlester, M. (2017). Geomagnetically induced currents: science, engineering and applications readiness. *Space Weather*, *15*, 828-856, https://doi.org/10.1002/2016SW001501

Radasky, W. A. (2011). Overview of the impact of intense geomagnetic storms on the US high voltage power grid. IEEE International Symposium on Electromagnetic Compatibility, 300-305, *IEEE Conference Publications*, New York, https://doi.org/10.1109/ISEM.2011.6038326

Ranganayaki, R. P. and Madden, T. R. (1980). Generalized thin sheet analysis in magnetotellurics: an extension of Price's analysis. *Geophys. J. R. Astr. Soc.*, *60*, 445-457. https://doi.org/10.1111/j.1365-246X.1980.tb04820.x

Rosenqvist, L. and Hall, O. (2019). Regional 3-D Modeling and Verification of geomagnetically induced currents in Sweden. *Space Weather*, *17*, 27-36. https://doi.org/10.1029/2018SW002084

Sakkas, V., Meju, M., Khan, M. A., Haak, V., Simpson, F. (2002). Magnetotelluric images of the crustal structure of the Chyulu Hills volcanic field, Kenya. *Tectonophysics*, 346, 3-4, 169-185. https://doi.org/10.1016/S0040-1951(01)00276-1

Schmucker, U. (1970). Anomalies of geomagnetic variations in the Southwestern United States. *Bull Scripps Inst. Ocean., University of California*, *13*. University of California Press Ltd, London, UK, pp 165. https://doi.org/10.1016/0031-9201(73)90061-7

Simpson, F. (1999). Stress and seismicity in the lower continental crust: a challenge to simple ductility and implications for electrical conductivity mechanisms. *Surveys in Geophysics*, *20*, 201-227. https://doi.org/10.1023/A:1006641922180

Simpson, F. (2000). A three-dimensional electromagnetic model of the southern Kenya Rift: departure from two-dimensionality as a possible consequence of a rotating stress field. *J. Geophys. Res.*, **105**, 19321-19334. https://doi.org/10.1029/2000JB900106

Simpson, F. (2002). A comparison of electromagnetic distortion and resolution of upper mantle conductivities beneath continental Europe and the Mediterranean using islands as windows. *Phys. Earth Planet. Inter.*, *129*, 117-130. https://doi.org/10.1016/S0031-9201(01)00264-3

Simpson, F. and Bahr, K. (2005). *Practical Magnetotellurics*, Cambridge University Press, London pp. 254. https://doi.org/10.1017/CBO9780511614095

Simpson, F. and Bahr, K. (2020). Magnetotelluric data from before, during and after the September 2017 magnetic storm at 7 sites in Scotland, National Geoscience Data Centre, British Geological Survey, Keyworth, UK (Dataset), https://doi.org/10.5285/59d3c54d-8179-4904-8ee7-1a81564ed893

Simpson, F., Haak, V., Khan, M. A., Sakkas, V., Meju, M. (1997). The KRISP-94 magnetotelluric survey of early 1995: first results, *Tectonophysics*, 278, 261-271. https://doi.org/10.1016/S0040-1951(97)00107-8

Simpson, F. and Warner M. (1998). Coincident magnetotelluric, P-wave and S-wave images of the deep continental crust beneath the Weardale granite, NE England: seismic layering, low conductance and implications against the fluids paradigm. *Geophys. J. Int.*, **133**, 419-434. https://doi.org/10.1046/j.1365-246X.1998.00512.x

Siripunvaraporn W., G. Egbert and Y. Lenbury, (2002). Numerical Accuracy of Magnetotelluric Modeling: A Comparison of Finite Difference Approximation, *Earth Planets Space*, *54*, 721-725. https://doi.org/10.1186/BF03351724

Siripunvaraporn W., G. Egbert, Y. Lenbury and M. Uyeshima, (2005), Three-Dimensional Magnetotelluric: Data Space Method, *Physics of the Earth and Planetary Interiors*, *150*, 3-14. https://doi.org/10.1016/j.pepi.2004.08.023

Tikhonov, A. N. (1950, reprinted 1986). On determining electrical characteristics of the deep layers of the Earth’s crust. In *Magnetotelluric Methods*, ed. K. Vozoff. Society of Exploration Geophysicists, Tulsa, pp. 2-3. ISBN 0931830362 9780931830365 0931830001 9780931830006

Viljanen, A. H., Nevanlinna, K., Pajunpää, K. and Pulkkinen, A. (2001). Time derivative of the horizontal geomagnetic field as an activity indicator. *Ann. Geophys.*, *19*, 1107-1118. https://doi.org/10.5194/angeo-19-1107-2001

Viljanen, A., Pulkkinen, A., Pirjola, R. Pajunpää, K., Posio, P. and Koistinen, A. (2006). Recordings of geomagnetically induced currents and a nowcasting service of the Finnish natural gas pipeline system. *Space Weather*, *4*, https://doi.org/10.1029/2006SW000234

Viljanen, A., Pirjola, R., Wik, M., Ádám, A., Prácser, E., Sakharov, Y. and Katkalov, J. (2012). Continental scale modelling of geomagnetically induced currents. *J. Space Weather Space Clim.*, *2*, A17. https://doi.org/10.1051/swsc/2012017

Watermann, J. and Gleisner, H. (2009). Geomagnetic variations and their time derivatives during magnetic storms at different levels of intensity. *Acta Geophysica*, *59*, 197-208. https://doi.org/10.2478/s11600-008-0045-7

Zhang, T., and A. Schultz (1990), EXORCISE—An algorithm for detection of spurious values and prediction of missing data, Comput. Geosci., 16, 1027–1065. https://doi.org/10.1016/0098-3004(90)90048-X

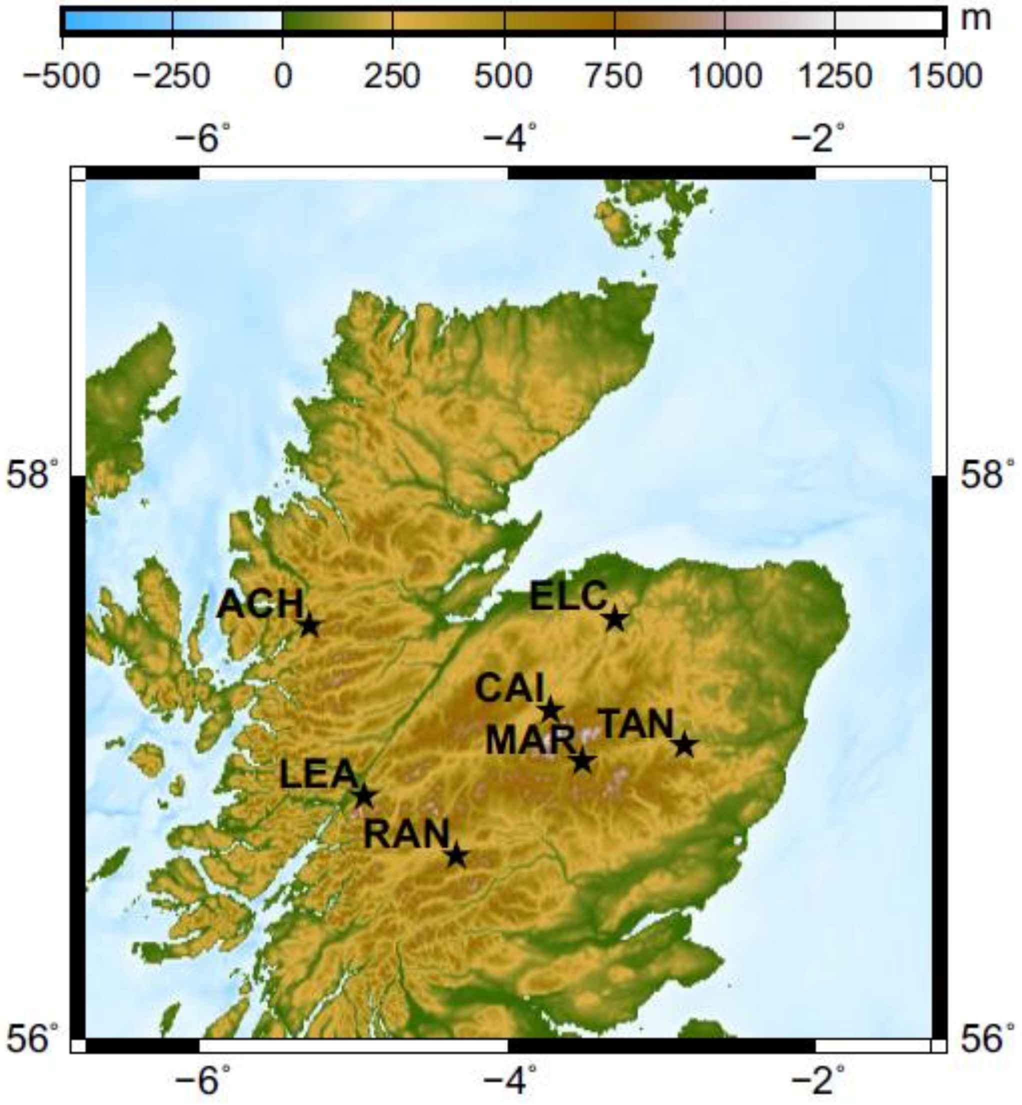

**Figure 1** Topographical map of northern Scotland showing positions of 7 sites at which MT data were recorded (Simpson and Bahr, 2020) during the September 2017 magnetic storm.

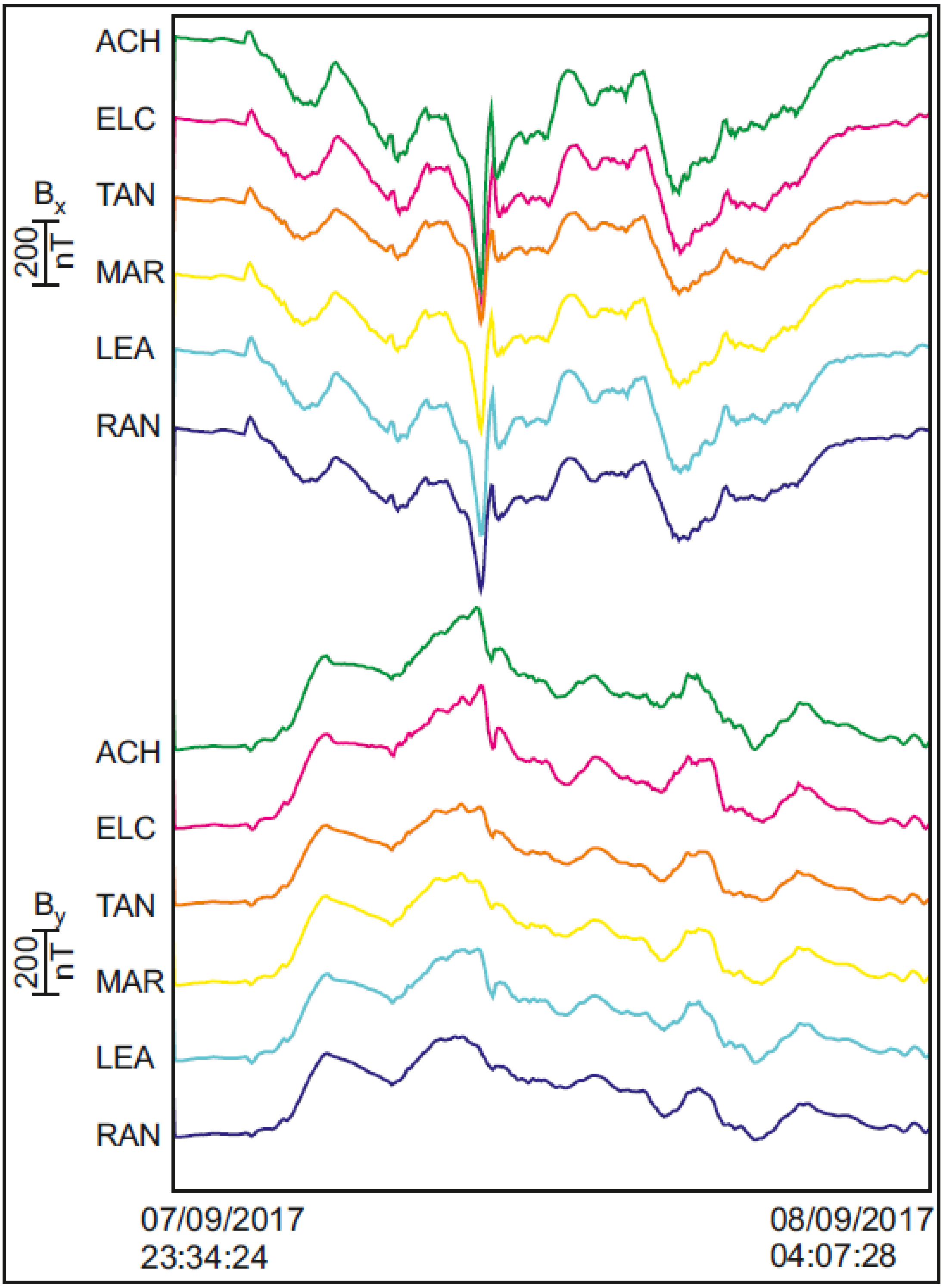

**Figure 2** Comparison of north-south ($B_x$) and east-west ($B_y$) magnetic fields recorded (Simpson and Bahr, 2020) during the 8th September 2017 magnetic storm at 6 of the 7 sites shown in Figure 1. Time series has been decimated to a sample rate of 32 s.

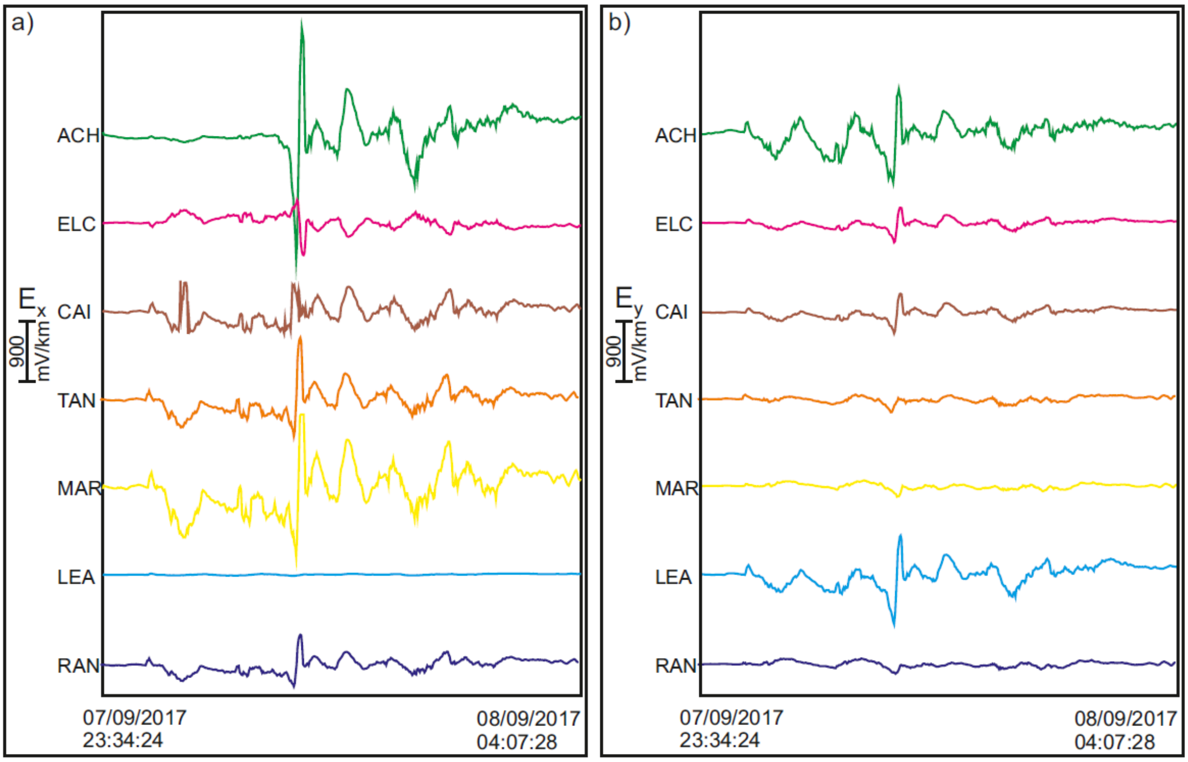

**Figure 3** Comparison of a) north-south ($E_x$) and b) east-west ($E_y$) electric fields recorded (Simpson and Bahr, 2020) during the 8th September 2017 magnetic storm at the 7 sites shown in Figure 1. Time series has been decimated to a sample rate of 32 s.

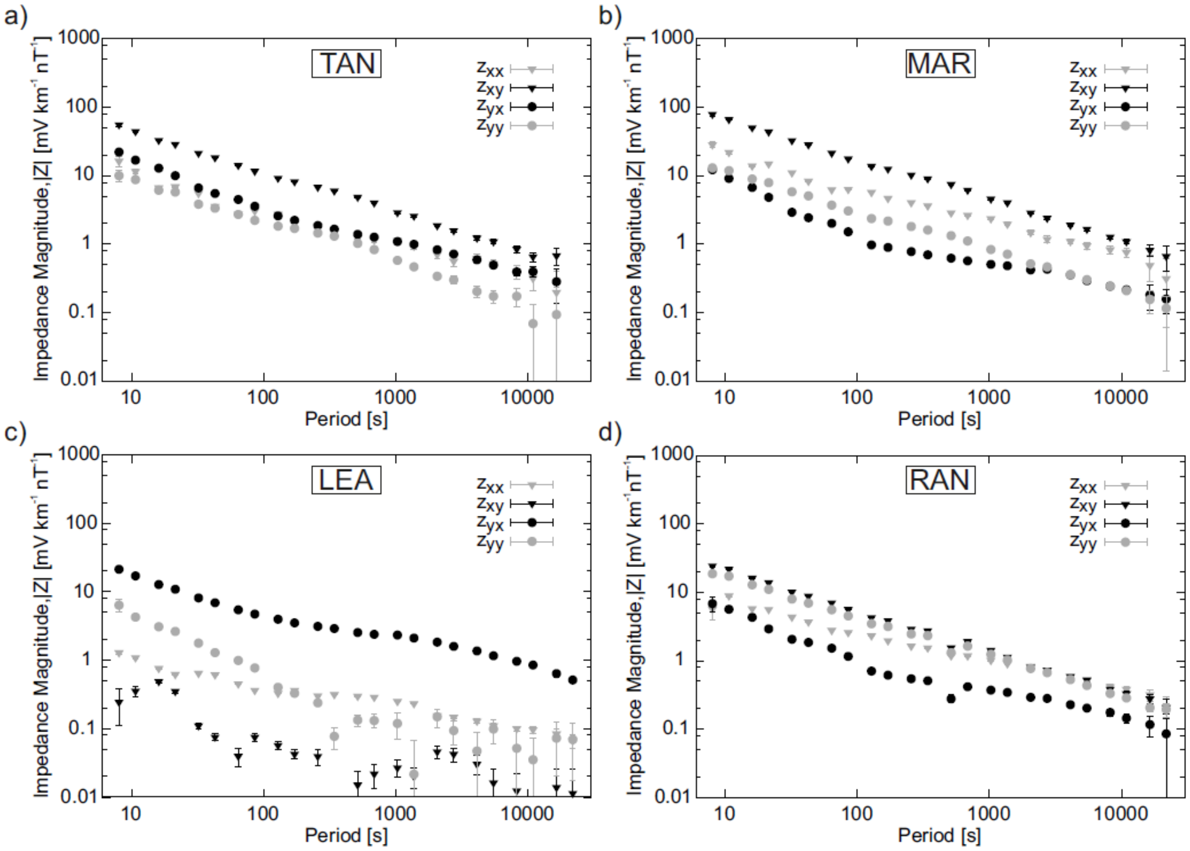

**Figure 4** Impedance magnitudes as a function of period for sites a) TAN; b) MAR; c) LEA; d) RAN (Figure 1).

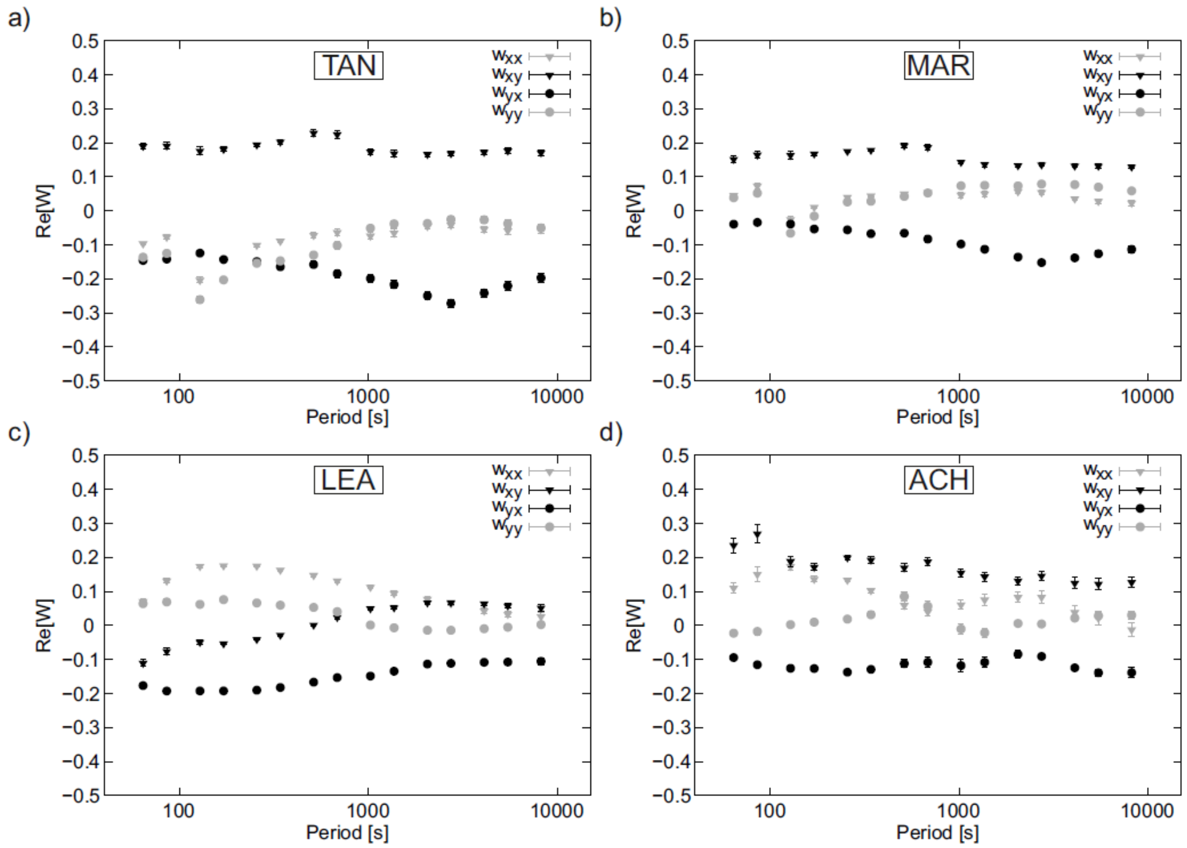

**Figure 5** Real components of the perturbation tensor, ***W***, at the 4 sites a) TAN; b) MAR; c) LEA; d) ACH derived relative to site RAN (Figure 1).

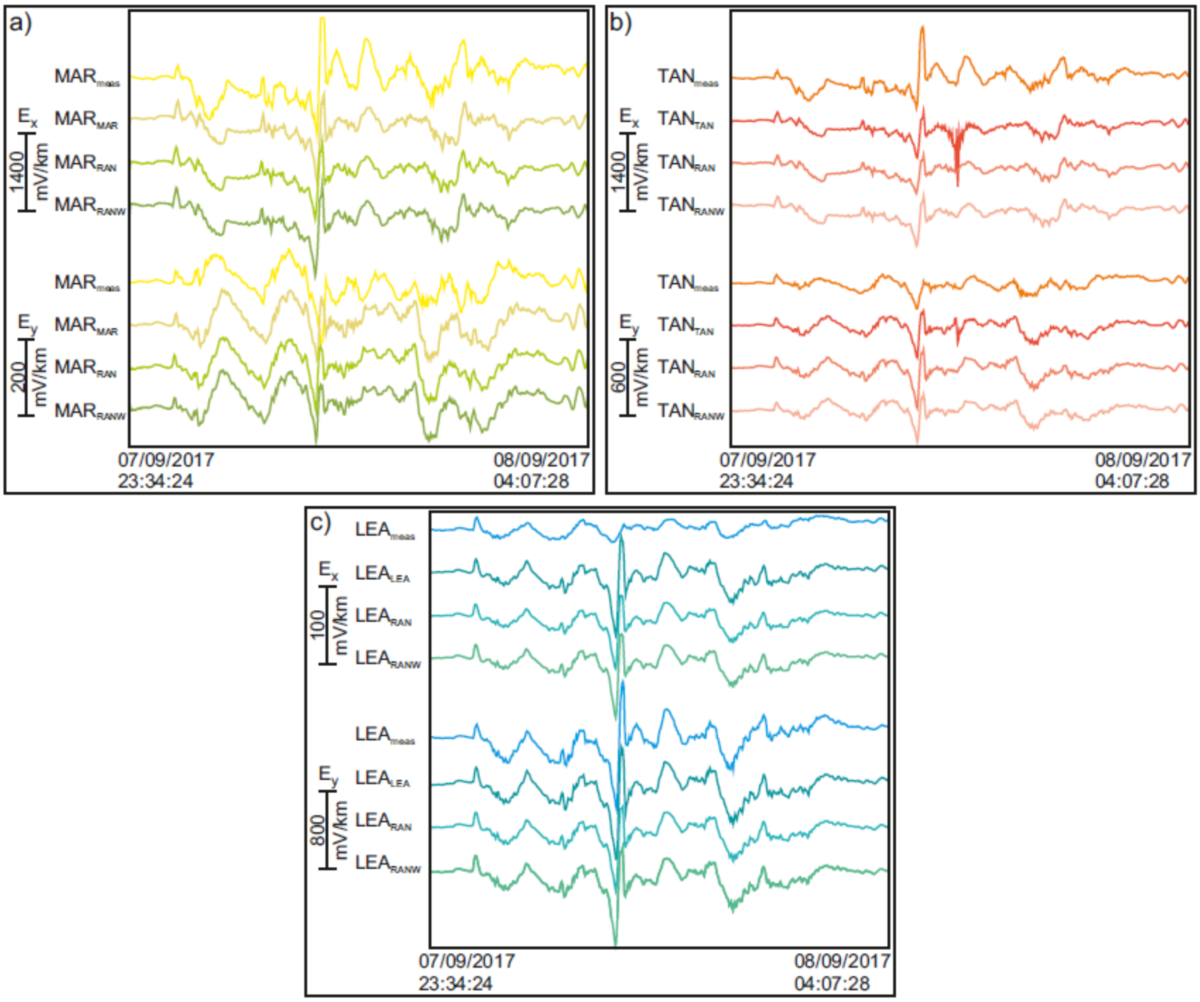

**Figure 6** Comparison of measured (Simpson and Bahr, 2020) and nowcasted north-south ($E_x$) and east-west ($E_y$) electric fields during the 8th September 2017 storm at a) MAR; b) TAN; c) LEA. Subscript "meas" denotes measured electric field, site name as subscript denotes the electric field nowcasted using the site's magnetic field and impedance tensor, subscript "RAN" denotes electric field nowcasted using the magnetic fields recorded at RAN and the site's impedance tensor, subscript "RANW" denotes electric fields nowcasted using the magnetic fields recorded at RAN and the site's modified impedance tensor that includes the perturbation-tensor correction for horizontal magnetic-field gradients between RAN and the site.

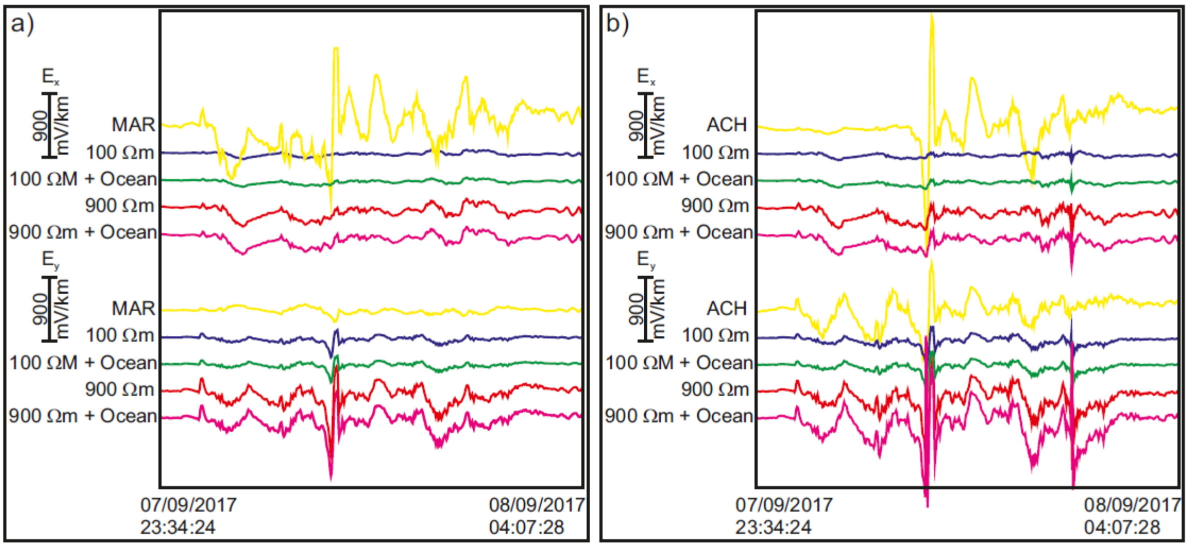

**Figure 7** Comparison of measured (yellow; Simpson and Bahr, 2020) and modelled, north-south ($E_x$) and east-west ($E_y$) electric fields during the 8th September 2017 storm at a) MAR and b) ACH. Modelled electric fields were obtained using the magnetic field recorded (Simpson and Bahr, 2020) at MAR or ACH, respectively, during the September 2017 storm and the impedances modelled at MAR or ACH, respectively, for the cases of models containing either a 100-Ωm half-space (blue), a 100-Ωm half-space plus ocean bathymetry (green), a 900-Ωm half-space (red), a 900-Ωm half-space plus ocean bathymetry (pink). Notice that there are significant discrepancies between features seen in the measured and modelled time series.

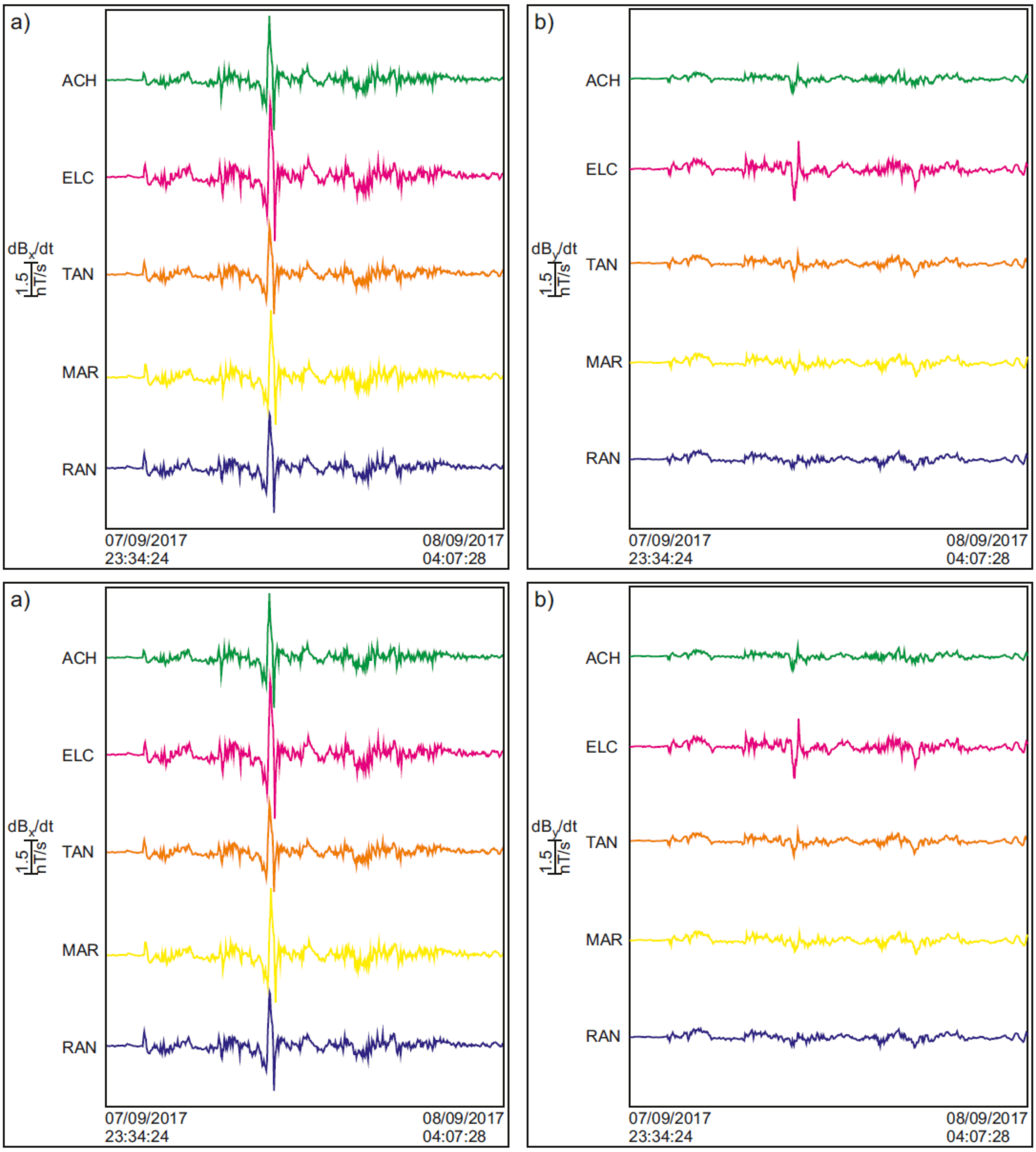

**Figure 8** Time derivatives of a) the north-south ($B_x$) magnetic field; b) the east-west ($B_y$) magnetic field at 4 sites for the same time window as the measured electric fields shown in Figure 3.

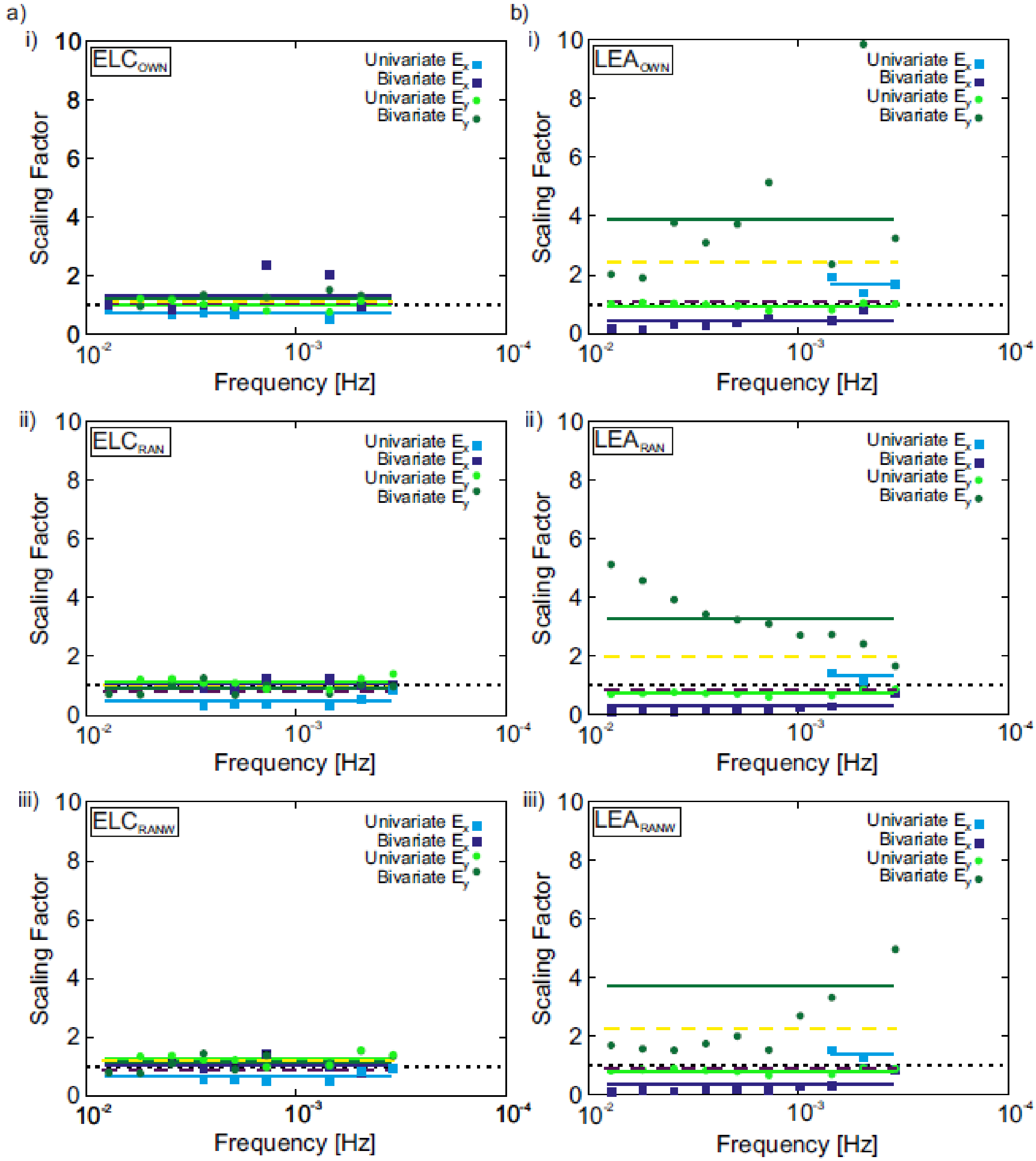

**Figure 9** Scatter plots of univariate and bivariate scaling factors for sites a) ELC and b) LEA between measured electric fields (Simpson and Bahr, 2020) and electric fields obtained from nowcasting using i) local magnetic fields; ii) magnetic fields from RAN; iii) magnetic field from RAN with perturbation-tensor correction. Solid horizontal lines show averages for the scatter plots of corresponding color. Dashed horizontal lines (purple $E_x$; yellow $E_y$) show the combined averages of the univariate and bivariate analyses.

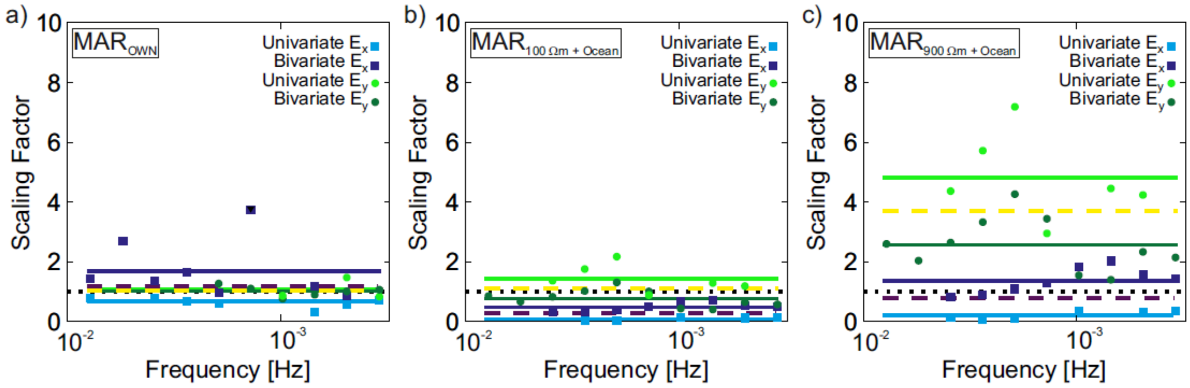

**Figure 10** Scatter plots of univariate and bivariate scaling factors for site MAR between measured electric fields (Simpson and Bahr, 2020) and electric fields obtained from nowcasting using locally-measured magnetic fields (Simpson and Bahr, 2020) and a) measured impedances; b) impedances derived from model representing 3D ocean bathymetry underlain by a 100-Ωm half-space; c) impedances derived from model representing 3D ocean bathymetry underlain by a 900-Ωm half-space. Solid horizontal lines show averages for the scatter plots of corresponding color. Dashed horizontal lines (purple $E_x$; yellow $E_y$) show the combined averages of the univariate and bivariate analyses.

**Table 1** Measured and nowcasted, maximum peak-to-peak, electric-field magnitudes (to the nearest mV) in a) north-south ($E_x$) and b) east-west ($E_y$) directions during the 8th September 2017 magnetic storm at the 7 sites shown in Figure1. Errors are less than 3% based on error propagation from measured impedances. Percentages shown in brackets are nowcasted magnitudes relative to measured magnitudes.

a) $E_x$ maximum peak-to-peak magnitudes

| Site | Measured (mV/km) | Nowcast from own magnetic field (mV/km) | Nowcast from RAN magnetic field (mV/km) | Nowcast from RAN magnetic field with ***W*** correction (mV/km) |
|---|---|---|---|---|
| ACH | 3631 | 853 (24%) | 439 (12%) | 510 (14%) |
| CAI | 738 | - | 663 (90%) | 945 (128%) |
| ELC | 852 | 653 (77%) | 341 (40%) | 496 (58%) |
| LEA | 29 | 133 (451%) | 97 (331%) | 112 (380%) |
| MAR | 2130 | 1635 (77%) | 1379 (65%) | 1690 (79%) |
| TAN | 1528 | 845 (55%) | 758 (50%) | 923 (60%) |
| RAN | 824 | 619 (75%) | 619 (75%) | 619 (75%) |

b) $E_y$ maximum peak-to-peak magnitudes

| Site | Measured (mv/km) | Nowcast from own magnetic field (mV/km) | Nowcast from RANN magnetic field (mV/km) | Nowcast from RANN magnetic field with ***W*** correction (mV/km) |
|---|---|---|---|---|
| ACH | 1469 | 2273 (155%) | 1483 (101%) | 1495 (102%) |
| CAI | 614 | - | 396 (64%) | 448 (73%) |
| ELC | 532 | 623 (117%) | 362 (68%) | 394 (74%) |
| LEA | 1366 | 1155 (85%) | 909 (67%) | 1061 (78%) |
| MAR | 252 | 185 (73%) | 195 (77%) | 190 (75%) |
| TAN | 272 | 320 (118%) | 454 (167%) | 325 (120%) |
| RAN | 246 | 168 (68%) | 168 (68%) | 168 (68%) |

**Table 2** Measured and modelled, maximum peak-to-peak, electric-field magnitudes (to the nearest mV) in a) north-south ($E_x$) and b) east-west ($E_y$) directions during the 8th September 2017 magnetic storm at 5 of the sites shown in Figure 1.

a) $E_x$ maximum peak-to-peak magnitudes

| Site | Measured (mV/km) | 100 Ωm Half-Space (mV/km) | 100 Ωm Half-Space + 3D Ocean (mV/km) | 900 Ωm Half-Space (mV/km) | 900 Ωm Half-Space + 3D Ocean (mV/km) |
|---|---|---|---|---|---|
| ACH | 3631 | 88 | 138 | 366 | 391 |
| LEA | 29 | 71 | 127 | 310 | 426 |
| MAR | 2130 | 99 | 94 | 250 | 275 |
| TAN | 1528 | 86 | 89 | 252 | 264 |
| RAN | 824 | 91 | 84 | 217 | 232 |

b) $E_y$ maximum peak-to-peak magnitudes

| Site | Measured (mV/km) | 100 Ωm Half-Space (mV/km) | 100 Ωm Half-Space + 3D Ocean (mV/km) | 900 Ωm Half-Space (mV/km) | 900 Ωm Half-Space + 3D Ocean (mV/km) |
|---|---|---|---|---|---|
| ACH | 1469 | 623 | 630 | 1746 | 2423 |
| LEA | 1366 | 512 | 503 | 1456 | 2041 |
| MAR | 252 | 401 | 392 | 1284 | 1204 |
| TAN | 272 | 338 | 346 | 984 | 1080 |
| RAN | 246 | 357 | 371 | 1056 | 1217 |

**Table 3** Peak-to-peak time derivatives of the storm-time horizontal magnetic fields recorded at 4 MT sites (Simpson and Bahr, 2020) and scaling factors required to match the measured peak-to-peak electric-field magnitudes given in Table 1.

| Site | $dB_y/dt$ (nT/s) | Scaling factor to measured $E_x$ | $dB_x/dt$ (nT/s) | Scaling factor to measured $E_y$ |
|---|---|---|---|---|
| ELC | 2.71 | 314 | 6.45 | 83 |
| MAR | 0.66 | 1248 | 4.54 | 54 |
| TAN | 1.35 | 1132 | 4.13 | 66 |
| RAN | 1.03 | 2068 | 5.13 | 49 |

**Table 4** Univariate and bivariate scaling factors between measured a) $E_x$ and b) $E_y$ fields obtained from nowcasting using local magnetic field, magnetic field from RAN and magnetic field from RAN with perturbation-tensor correction.

a) $E_x$ scaling factors

| Site | Scaling factor from own magnetic field (mV/km) | | | Scaling factor from RAN magnetic field (mV/km) | | | Scaling factor from RAN magnetic field with ***W*** correction (mV/km) | | |
|---|---|---|---|---|---|---|---|---|---|
| | Univ. | Biv. | Average | Univ. | Biv. | Average | Univ. | Biv. | Average |
| ACH | 0.236 | 0.241 | 0.239 | 0.278 | 0.271 | 0.274 | 0.319 | 0.304 | 0.311 |
| ELC | 0.753 | 1.328 | 1.040 | 0.498 | 1.086 | 0.792 | 0.675 | 1.058 | 0.866 |
| LEA | 1.705 | 0.473 | 1.089 | 1.325 | 0.319 | 0.822 | 1.421 | 0.353 | 0.887 |
| MAR | 0.678 | 1.695 | 1.186 | 0.668 | 1.163 | 0.915 | 0.716 | 1.097 | 0.906 |
| TAN | 0.571 | 1.147 | 0.859 | 0.784 | 1.121 | 0.953 | 0.718 | 1.066 | 0.892 |
| RAN | 0.680 | 0.793 | 0.737 | 0.680 | 0.793 | 0.737 | 0.680 | 0.793 | 0.737 |

b) $E_y$ scaling factors

| Site | Scaling factor from own magnetic field (mV/km) | | | Scaling factor from RAN magnetic field (mV/km) | | | Scaling factor from RAN magnetic field with ***W*** correction (mV/km) | | |
|---|---|---|---|---|---|---|---|---|---|
| | Univ. | Biv. | Average | Univ. | Biv. | Average | Univ. | Biv. | Average |
| ACH | 0.933 | 1.694 | 1.314 | 1.120 | 1.006 | 1.063 | 1.190 | 1.113 | 1.151 |
| ELC | 1.016 | 1.228 | 1.122 | 1.136 | 0.906 | 1.021 | 1.265 | 1.144 | 1.205 |
| LEA | 0.961 | 3.900 | 2.430 | 0.715 | 3.270 | 1.993 | 0.812 | 3.738 | 2.275 |
| MAR | 1.060 | 1.021 | 1.041 | 1.854 | 1.029 | 1.441 | 1.384 | 1.071 | 1.227 |
| TAN | 1.183 | 0.945 | 1.064 | 1.641 | 1.024 | 1.332 | 1.318 | 0.943 | 1.135 |
| RAN | 1.025 | 0.952 | 0.988 | 1.025 | 0.952 | 0.988 | 1.025 | 0.952 | 0.988 |